

Variation of the fundamental band gap nature in curved two-dimensional WS₂

*E. Blundo[‡], M. Felici[‡], T. Yildirim[†], G. Pettinari[◇], D. Tedeschi[‡], A. Miriametro[‡], B. Liu[†],
W. Ma[†], Y. Lu,^{†#} and A. Polimeni^{‡,*}*

[‡] Dipartimento di Fisica, Sapienza Università di Roma, 00185 Roma, Italy

[†] Research School of Electrical, Energy and Materials Engineering, College of Engineering and
Computer Science, The Australian National University, Canberra, ACT 2601, Australia

[◇] Institute for Photonics and Nanotechnologies, National Research Council, 00156 Roma, Italy

[#] ARC Centre of Excellence in Future Low-Energy Electronics Technologies (FLEET) ANU
node, Canberra, ACT 2601, Australia

We report a strain-induced direct-to-indirect band gap transition in mechanically deformed WS₂ monolayers (MLs). The necessary amount of strain is attained by proton irradiation of bulk WS₂ and the ensuing formation of one-ML-thick, H₂-filled domes. The electronic properties of the curved MLs are mapped by spatially- and time-resolved micro-photoluminescence revealing the mechanical stress conditions that trigger the variation of the band gap character. This general phenomenon, also observed in MoS₂ and WSe₂, further increases our understanding of the

electronic structure of transition metal dichalcogenide MLs and holds a great relevance for their optoelectronic applications.

KEYWORDS Transition metal dichalcogenides, strain, hydrogen, photoluminescence, FEM calculations

The properties of solids are very sensitive to variations in bond length ensuing a mechanical deformation or stress. This is especially true in the case of two-dimensional (2D) crystals (such as graphene, hexagonal-BN and transition metal dichalcogenide, TMD, monolayers, MLs) due to their all-surface nature¹. Particularly appealing in TMD MLs is the strong coupling between the valley/spin/orbital degrees of freedom and the lattice structure, reflected in the strong response of their electronic², transport³, and optical⁴ properties to strain. In particular, non-uniform strains turn out to be extremely relevant: On the one hand, strain gradients in 2D-TMDs can lead to a coherent drift of photo-generated carriers, relevant for photon harvesting^{5,6}. On the other hand, a non-uniform strain gives rise to pseudo-electromagnetic fields enabling the observation of novel transport phenomena⁷.

In this letter, we report a study of the band gap character in mechanically-deformed WS₂ 2D crystals. The deformation follows the local blistering over a micron-sized region of the upper layer of bulk WS₂ flakes exposed to proton irradiation⁸. The resulting spherically-shaped MLs, hereafter named domes, host non-uniform and high strain fields, evaluated by finite-element method (FEM) calculations and consistently compared with micro-Raman measurements. Steady-state and time-resolved micro-photoluminescence (PL) mapping of the band gap states over the surface of a single dome unveils dramatic changes in the emission energy, intensity and decay time. Such changes are related to the built-in tensile strain of the dome and are ascribed to a strain-induced direct (K_{CB} - K_{VB})-to-indirect (K_{CB} - Γ_{VB}) band gap transition (CB and VB stand for conduction and valence band, respectively). The strain conditions that determine the cross-over of the VB Γ and K states are found. A similar behavior is also observed in MoS₂ and WSe₂.

The dome-shaped membranes under study were created from bulk MX₂ flakes (where M: W or Mo, and X: S, Se or Te), which were mechanically exfoliated on Si substrates and then

proton-irradiated with a low-energy beam^{8,9}. Here, we focus on WS₂. The accelerated protons penetrate through the flake surface and H₂ forms just one layer beneath the surface, as described in Ref. 8. As a consequence of the balance between the gas expansion, the van der Waals forces holding the S-W-S planes together and the material's elastic properties, localized swelling of just one ML takes place, resulting in the formation of atomically-thin and spherically-shaped domes [see the atomic force microscope, AFM, image in Fig. 1(a)]. The domes cage highly-pressurized H₂ and are durable thanks to the impermeability to H₂ of TMD MLs¹⁰. As shown in Fig. 1(a), domes with different size stud the flake's surface, nevertheless featuring an aspect ratio, $h_m/R=0.16\pm 0.02$, independent of R ^{8,11} (R is the footprint radius and h_m is the maximum height of the domes). The domes were characterized by micro-Raman and micro-PL experiments using a 532 nm laser as the excitation source. A diffraction grating monochromator coupled to a Si-CCD was used for spectral analysis of the signal. Time-resolved micro-PL was performed using a supercontinuum laser tuned at 532 nm with ~50 ps pulse width and 77.8 MHz repetition rate. The signal was time-analyzed by a Si APD with 250 ps temporal resolution. Spatially-resolved optical measurements were performed in back-scattering configuration via a 100× objective with NA=0.9, resulting in a laser spot with standard deviation equal to $0.23\pm 0.01 \mu\text{m}$ ¹². Finally, the strain tensor over the dome's surface was computed via FEM calculations.

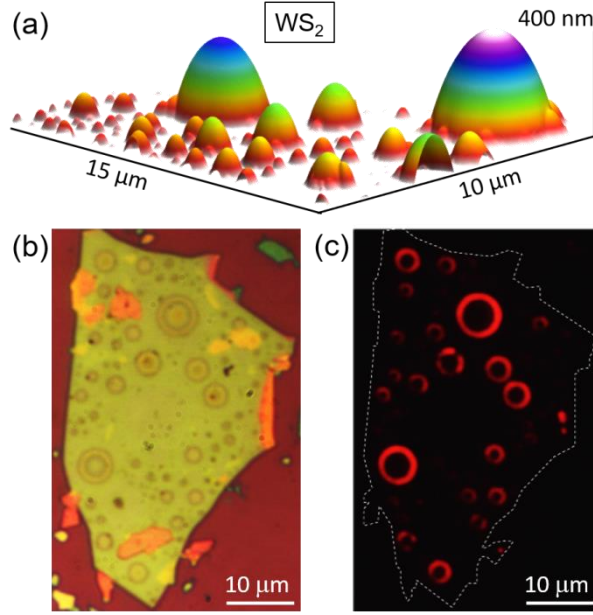


FIG. 1. (a) 3D AFM image of a bulk WS_2 flake irradiated with protons (dose $d_H=4\times 10^{16}$ protons/cm²), showing the formation of almost-perfectly-spherical domes. (b) Optical image of a WS_2 flake, where many relatively large domes formed after proton-irradiation ($d_H=5\times 10^{16}$ protons/cm²). (c) Laser-excited red luminescence coming from the same flake shown in panel (b).

Fig. 1(b) shows the optical microscope image of a proton-irradiated WS_2 flake acquired with a $50\times$ (NA=0.5) objective. The outer circular borders locate the domes' footprint while the internal patterns of each dome are due to interference effects between the light reflected by the dome top surface and the flat WS_2 flake underneath⁸. Fig. 1(c) shows an optical image of the same flake, excited by a defocused 532 nm laser. The image was acquired at room temperature by filtering the laser out, thus letting the red luminescence (at ~ 690 nm) generated by the domes be revealed. Peculiarly, the brightly emitting region is restricted to an outer ring-like area independently of the dome footprint. This excludes interference (which would be largely dependent on the dome size) to be at the origin of the observed luminescence pattern, differently from what recently reported in WS_2 bubbles obtained after annealing of chemical-vapor-deposition-grown MLs¹³. In that work, interference effects are likely enhanced by the SiO_2 substrate located right beneath the ML bubbles and strongly modulate the emission. On the contrary, in the present case, the

peculiar ring-like emitting area stems from the strain field acting over the domes, as detailed in the following.

To model the spatial evolution of the strain tensor and the height profile of the domes we performed FEM calculations within the framework of the nonlinear membrane theory^{14,15,16}. The AFM-derived radius and height of the domes and the elastic properties of the material were used as input parameters. Fig. 2(a) (left axis) successfully compares the experimental (circles) and calculated (solid line) height profile along a radius ($0 \leq r \leq R$, where r is the position with respect to the center) of the WS_2 dome, whose AFM image is shown in the inset. The right axis of Fig. 2(a) displays the calculated r dependence of the principal components of the strain tensor — namely, along the circumferential (ε_t) and radial (ε_r) in-plane directions¹⁴ and along the perpendicular (ε_z) out-of-plane direction. At the dome's summit, the (tensile) strain is isotropic biaxial ($\varepsilon_t = \varepsilon_r = 2.09\%$) in agreement with Hencky's model^{4,14,16,17}, whereas at the dome edges —where $\varepsilon_t = 0$ — strain is uniaxial. The negative value of ε_z all over the surface is caused by the membrane thinning following the in-plane tensile strain. The strain field across the dome is expected to induce remarkable changes in the electronic properties of the curved TMD membrane^{5,18,19,20,21,22,23,24,25}, giving rise to the peculiar phenomenology displayed in Fig. 1(c). Spatially-resolved micro-PL/Raman measurements were then performed on the dome shown in Fig. 2(a), which was chosen since its size ($R = 2.85 \mu\text{m}$) is much larger than the probing laser spot ($0.23 \mu\text{m}$)¹², thus minimizing diffraction effects. However, it is important to note that the dome aspect ratio and, consequently, the strain distribution remain unchanged with the dome size⁸ ensuring the general significance of the following results.

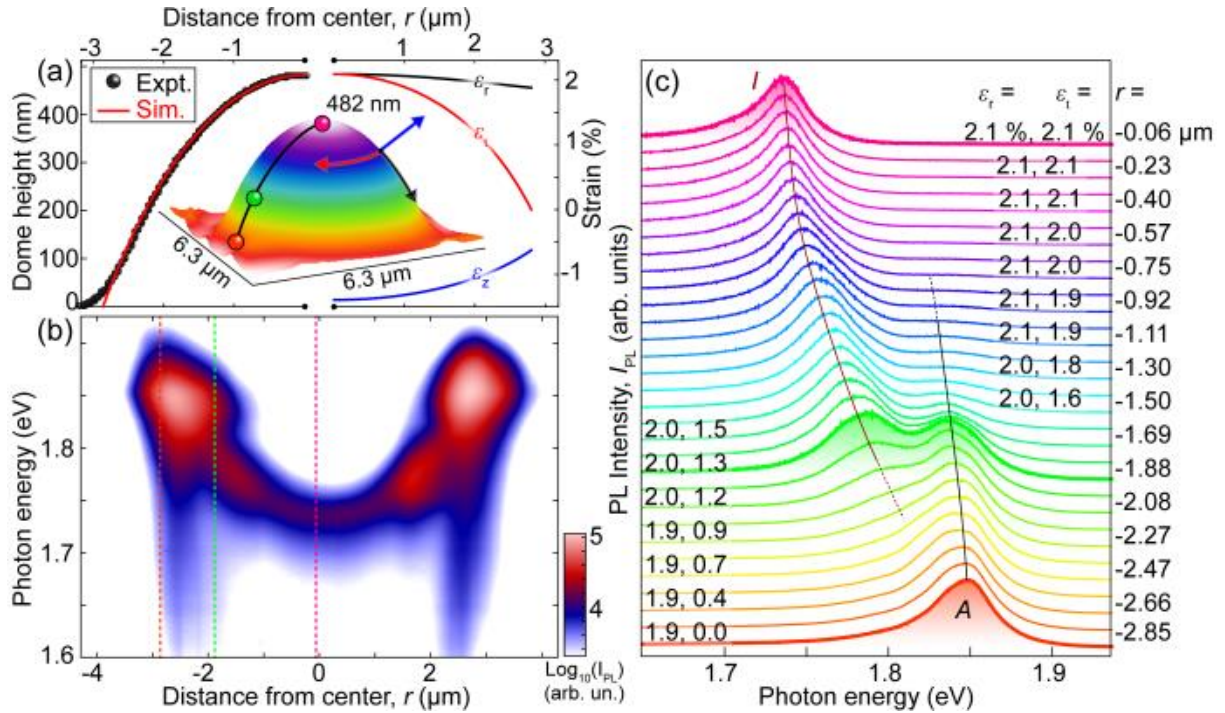


FIG.2. (a) Left: Height profile of a WS₂ dome formed after irradiation with 4×10^{16} protons/cm², measured by AFM (black dots; the AFM image is shown as inset), and computed by FEM calculations (solid red line). Right: Dependence along the dome radius of the strain tensor components, represented as color-coded arrows in the inset. The three dots (purple: top; green: intermediate; orange: edge) correspond to the positions displayed as dashed lines in (b) and to the shadowed spectra in (c). (b) Micro-PL scan along a diameter of the dome displayed in (a), performed at 297 K. The horizontal axis indicates the laser spot position with respect to the dome center, the vertical axis indicates the emitted photon energy. The base-10 logarithm of the micro-PL intensity is shown in a false color scale. (c) Normalized emission spectra of the dome as the laser spot is scanned from the dome's left edge (bottom) to its apex (top). Spectra are labeled with the laser spot position and with the values of the radial and circumferential strain components. The solid lines follow the energy shift of the direct (A, black line) and indirect (I, red line) exciton transition.

To begin with, the micro-Raman measurements described in the Supplemental Material¹⁶ show a progressive softening of the in-plane and out-of-plane vibrational modes while moving from the edge towards the center of the dome, in agreement with the expected tensile-strain increase^{13,26,27}. However, the full extent of the effects of strain on the optoelectronic properties of TMD MLs can only be appreciated by looking at the dome's PL emission. Fig. 2(b) depicts a room temperature micro-PL scan taken along a diameter of the dome displayed in the inset of panel (a). The vertical axis indicates the energy of the emitted photons, while the base-10 logarithm of the PL intensity is shown in a false color scale. On moving from the edge toward

the summit of the dome, the marked red-shift of the emission wavelength is accompanied by an equally striking decrease (about a factor of 20) of the PL intensity. Figure 2(c) describes in more detail the dramatic changes of the emission spectra from the dome's edge ($r = -2.85 \mu\text{m}$) to the dome's center ($r = -0.06 \mu\text{m}$). Each spectrum is labelled also with the pertinent values of the radial and circumferential strain components [see panel (a)]. The micro-PL spectra recorded close to the edge are dominated by the direct ($K_{\text{CB}}-K_{\text{VB}}$) band gap exciton (A), whose energy (equal to 2.00 eV in a strain-free reference WS_2 ML⁸) is red-shifted by the tensile strain exerted on the dome. As the excitation laser moves toward the center, the direct exciton keeps red-shifting and concomitantly a new, less intense band, labeled I , takes over and eventually dominates the spectrum. We ascribe this band to the $K_{\text{CB}}-\Gamma_{\text{VB}}$ *indirect* band gap exciton. In fact, as predicted by numerous theoretical works^{5,18,19,21,22,23,24,25} the presence of strain in TMD MLs should result in a significant reordering of the energies of the critical points of the band structure. In particular, for tensile biaxial strains $\varepsilon \gtrsim 1\%$ in WS_2 ^{18,19,21,22,23,25}, the valence band maximum should change from the K to the Γ point of the reciprocal space. Even though this change (*i*) is expected to occur for values of ε that are well within reach of current strain modulation techniques^{28,29,30,31}, and (*ii*) should result in rather dramatic variations of the optical properties of the material, the currently available experimental evidence of this direct-to-indirect transition is either not particularly apparent^{32,33} or absent^{13,29,30,31}. This is possibly due to a less-than-perfect adhesion between the sample and the strain-inducing devices employed in some of the previous studies, resulting in an incomplete transfer of the applied stress to the TMD ML. In the present work, however, this is not an issue, as large biaxial strains—in the range between 1 - 3% —are induced by the pressure exerted on the TMD ML by the H_2 gas trapped and perfectly sealed within the dome.

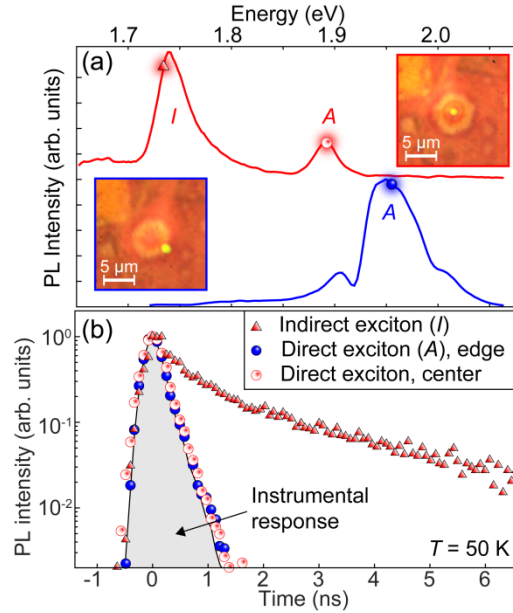


FIG.3. (a) $T=50$ K micro-PL spectra recorded at the center (red) and edge (blue) of a WS_2 dome. The insets are optical microscope images of the dome, showing the laser spot position corresponding to each spectrum. The symbols superimposed to the spectra indicate the energy at which the signal temporal decay shown in panel (b) was recorded. (b) Temporal evolution of the micro-PL signal relative to the specific photon energy and position on the dome highlighted in panel (a). The gray-shaded area refers to the exciting laser decay curve and sets the temporal resolution.

To confirm the previous attributions, we investigated the temporal decay of the micro-PL signal of WS_2 domes. These were cooled down at 50 K to minimize the contribution of non-radiative decay channels³⁴. Interestingly, the reduction of the dome's volume at cryogenic temperatures⁸—due to the contraction of the H_2 gas trapped inside the dome—is nearly brought to a halt by the deposition of a thin methylpentane layer on the sample surface (see Supplemental Material), thus making it possible to spatially resolve the PL signal from different zones of the dome. Fig. 3(a) shows the micro-PL spectra of a WS_2 dome recorded at the edge (where the A exciton dominates) and center (where the I exciton can be observed along with the red-shifted A exciton recombination); see pictures in the insets. Fig. 3(b) shows the micro-PL decay curve relative to the different transitions displayed in (a). Most notably, the A and I excitons exhibit largely different temporal behaviors: The decay time of the A exciton is instrument-limited (<250

ps) consistent with other reports^{34,35}. Instead, the *I* exciton shows a much longer temporal decay that can be fitted by a double exponential function with two decay times equal to (0.40 ± 0.06) ns and (2.9 ± 0.7) ns, which clearly points to an indirect optical transition³⁵.

We now establish the strain conditions that induce the K- Γ crossover in the VB. This is an especially important aspect with regard to the optoelectronic properties of TMD MLs and to the enormous potential that mechanical stress holds to engineer those properties. For instance, application of a seamless gradient of strain in these materials could be exploited as an efficient broad-band concentrator of photogenerated carriers in flexible solar cells⁵. Nevertheless, the occurrence of a strain-induced transition in the band gap character may affect both the absorption/emission properties and the carrier dynamics characteristics of devices based on TMD MLs. Furthermore, in the present case, the strain gradient enables the spatial concentration of long-lived *k*-indirect excitons with potential benefit for creating excitonic Bose condensates³⁶.

Figure 4(a) illustrates a micro-PL experiment performed on a single dome, highlighting the relevant physical processes discussed next. Panel (b) shows the peak energy $E_{A,I}$ of the *A* and *I* excitonic transitions derived from the same dome of Fig. 2 as a function of the “in-plane” strain $\varepsilon_p = \varepsilon_r + \varepsilon_t$. This choice is grounded on the hypothesis that each of the two planar strain components brings a similar effect on the ML band gap¹⁸. Moreover, for biaxially strained TMDs $\varepsilon_z = -\frac{D_{13}}{D_{33}}\varepsilon_p$, where D_{13} and D_{33} are the pertinent components of the elasticity matrix^{16,37}. Thus, as discussed in Supplemental Material¹⁶ the strain dependence of the energies of the *A* and *I* excitons can be written as

$$E_{A,I}(\varepsilon_p) = E_{A,I}(0) - \Delta_{A,I} \cdot \varepsilon_p, \quad (1)$$

where $\Delta_{A,I}$ is the shift rate with strain of the *A* (*I*) exciton. To correctly interpret the data shown in Fig. 4(b), however, we also have to consider that the continuous variation of the strain field on

the dome surface [Fig. 2(a)]—and hence the progressive decrease of the band gap energy from the dome edge toward its center—leads excitons to drift toward the minimum energy available within their diffusion length before recombining [see panel (a)]^{5,6}.

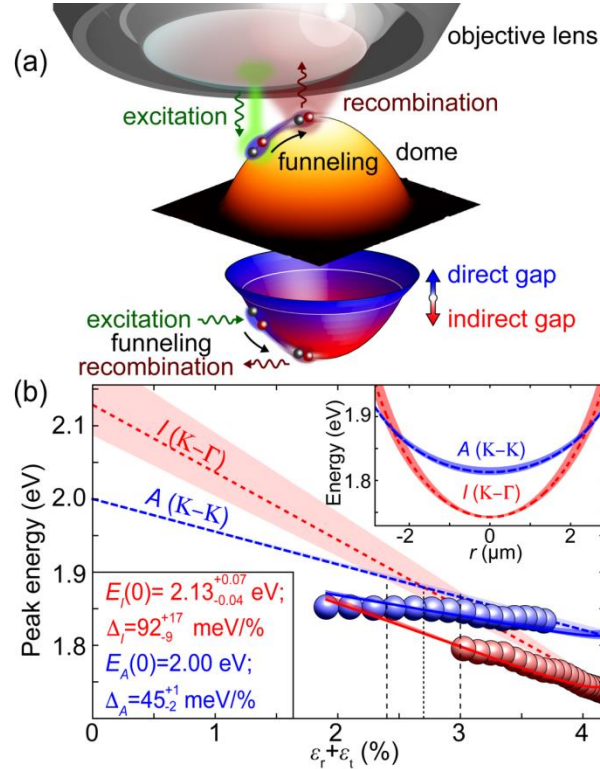


FIG. 4. (a) Sketch of a micro-PL experiment (excitation+recombination) on a single WS₂ dome (whose AFM image is shown in shaded orange), wherein an exciton drifts over the dome strain distribution (funnel effect^{5,6}). The blue-red paraboloid provides a correspondence between the dome AFM image and the exciton energy, highlighting the direct-indirect transition region (see below). (b) Dependence of the energy of the direct (blue dots) and indirect (red dots) exciton transitions on the in-plane strain tensor, $\varepsilon_p = \varepsilon_r + \varepsilon_t$. The continuous blue/red lines (relative to the direct/indirect exciton) are fits based on Eq. (1), while also taking funneling [see panel (a)] into account. These fits entail linear dependences of the exciton energies on ε_p , which are displayed as dashed lines; the shaded areas enveloping each curve account for the uncertainty of our fitting procedure (see main text). In turn, these linear dependences yield the evolution of the direct and indirect exciton energy across the dome, plotted in the inset of panel (b) [the paraboloid sketched in (a) is also based on this evolution].

Such a funnel effect, combined with the finite exciting/collecting area of the objective, alters the correspondence between the coordinate r (and thus ε_p) and the exciton energy derived from the emission spectra⁶. The solid curves displayed in Fig. 4(b) result from a fit performed by taking into account the exciton funneling [see Supplemental Material¹⁶], while fixing the radius

of the collection area, R_c , to 2.5σ ($\sigma = 0.23 \mu\text{m}$ is the laser spot size¹²). The actual [*i.e.*, free from the funnel effect; see Eq. (1)], “linearized” strain dependence of the A (I) exciton is shown in Fig. 4(b) as a blue (red) dashed line. The surrounding shaded areas—covering the regions spanned by the trends computed for $2\sigma \leq R_c \leq 3\sigma$ —represent the uncertainty of our procedure. This analysis permits to set the direct-to-indirect band gap crossover point at $\varepsilon_p = (2.7 \pm 0.3)\%$ highlighted by vertical dashed lines in Fig. 4(b). Finally, the top-right inset in Fig. 4(b) provides the A and I exciton energy as a function of the dome radial coordinate. The displayed fits yield $\Delta_A = 45_{-2}^{+1} \text{ meV}/\varepsilon \%$, $E_I(0) = 2.13_{-0.04}^{+0.07} \text{ eV}$ and $\Delta_I = 92_{-9}^{+17} \text{ meV}/\varepsilon \%$ [$E_A(0)$ is fixed to 2.00 eV, the strain-free ML exciton energy]. These data compare rather favorably with the experimental^{30,38}, and theoretical^{18,19,21,22,23,25,39} ones as discussed in Ref. 16. We finally point out that we observed similar findings also in MoS_2 and WSe_2 ¹⁶. This gives to our results a particular relevance regarding the general electronic properties of TMD 2D crystals.

In conclusion, we investigated the intertwined strain and electronic properties of spherically-deformed TMD monolayers. We observed that sufficiently high tensile in-plane strains ($\varepsilon_p \sim 2.7\%$ in WS_2 -ML) turn a direct band gap material into an indirect-gap one. This general behavior, common to other TMDs—like MoS_2 and WSe_2 —must be considered when 2D crystal are to be employed in flexible optoelectronic devices, or possibly exploited for the observation of quantum many-body effects involving long-lived k -space indirect excitons³⁶.

AUTHOR INFORMATION

* corresponding author: antonio.polimeni@roma1.infn.it

Acknowledgements. We thank A. Surrente for comments and suggestions. We acknowledge support by Sapienza Università di Roma under the grants “Ricerche Ateneo” years 2017 and 2018 (A.P. and M.F.). M.F. and G.P. acknowledge support and funding from the Italian Ministry for Education, University and Research within the Futuro in Ricerca (FIRB) program (project DeLIGHTeD, Prot. RBFR12RS1W). This project has also received funding from the European Union’s Horizon 2020 research and innovation program No. 641899. We acknowledge fund support from Australian Research Council (ARC) (numbers DE140100805 and DP180103238), and ARC Centre of Excellence in Future Low-Energy Electronics Technologies (project number CE170100039).

-
- ¹ Z. Dai, L. Liu and Z. Zhang, Strain Engineering of 2D Materials: Issues and Opportunities at the Interface, *Adv. Mat.* 1805417 (2019).
- ² H. Ochoa, R. Zarzuela, and Y. Tserkovnyak, Emergent Gauge Fields from Curvature in single Layers of Transition-Metal Dichalcogenides, *Phys. Rev. Lett.* **118**, 026801 (2017).
- ³ J. Son, K.-H. Kim, Y. H. Ahn, H.-W. Lee, and J. Lee, Strain engineering of the Berry Curvature dipole and Valley Magnetization in Monolayer MoS₂, *Phys. Rev. Lett.* **123**, 036806 (2019)
- ⁴ D. Lloyd, X. Liu, J. W. Christopher, L. Cantley, A. Wadehra, B. L. Kim, B. B. Goldberg, A. K. Swan, and J. S. Bunch, Band gap engineering with ultralarge biaxial strains in suspended monolayer MoS₂, *Nano Lett.* **16**, 5836 (2016).
- ⁵ J. Feng, X. Qian, C.-W. Huang, and J. Li, Strain-engineered artificial atom as a broad-spectrum solar energy funnel, *Nat. Photon.* **6**, 866 (2012).
- ⁶ . A. Castellanos-Gomez, R. Roldan, E. Cappelluti, M. Buscema, F. Guinea, H. S. J. van der Zant, G. A. Steele, Local Strain Engineering in Atomically Thin MoS₂, *Nano Lett.* **13**, 5361-5366 (2013).
- ⁷ B. Amorim, A.Cortijo, F. de Juan, A. G. Grushin, F.Guinea, A.Gutiérrez-Rubio,H.Ochoa, V.Parente, R. Roldán, P. San-Jose, J. Schiefele, M.Sturla, M. A. H. Vozmediano, Novel effects of strains in graphene and other two dimensional materials, *Phys. Rep.* **617**, 1 (2016).
- ⁸ D. Tedeschi, E. Blundo, M. Felici, G. Pettinari, B. Liu, T. Yildirim, E. Petroni, C. Zhang, Y. Zhu, S. Sennato, Y. Lu, and A. Polimeni, Controlled Micro/Nanodome Formation in Proton-Irradiated Bulk Transition-Metal Dichalcogenides, *Adv. Mat.* (2019), in press, DOI: 10.1002/adma.201903795.

-
- ⁹. R. Trotta, A. Polimeni, F. Martelli, G. Pettinari, M. Capizzi, L. Felisari, S. Rubini, M. Francardi, A. Gerardino, P. C. M. Christianen, J. C. Maan, *Adv. Mater.* **23**, 2706-2710 (2011).
- ¹⁰. Seel, M. & Pandey, R. Proton and hydrogen transport through two-dimensional monolayers. *2D Mater.* **3**, 025004 1-17 (2016).
- ¹¹. E. Khestanova, F. Guinea, L. Fumagalli, A. Geim, I. Grigorieva, Universal shape and pressure inside bubbles appearing in van der Waals heterostructures, *Nat. Commun.* **7**, 12587. (2016).
- ¹² The laser spot size resulting from the NA=0.9 objective employed for micro-Raman and micro-PL mapping was experimentally determined as follows: the laser was scanned across a reference sample, lithographically patterned with features of known width (1 μm). The intensity of the reflected light was fitted with the ideal reflectance profile, convolved with a Gaussian peak. The standard deviation of this peak, obtained as a fitting parameter, provides our estimate of $\sigma=0.23\pm 0.01$ μm .
- ¹³ Z. Jia, J. Dong, L. Liu, A. Nie, J. Xiang, B. Wang, F. Wen, C. Mu, Z. Zhao, B. Xu, Y. Gong, Y. Tian, and Z. Liu, Photoluminescence and Raman Spectra oscillations Induced by laser Interference in Annealing-Created Monolayer WS₂ bubbles, *Adv. Opt. Mat.* **7**, 1801373 (2019).
- ¹⁴. P. Wang, W. Gao, Z. Cao, K. M. Liechti, R. Huang, *J. Appl. Mech.* **80**, 040906 (2013).
- ¹⁵. P. Wang, W. Gao, Z. Cao, K. M. Liechti, and R. Huang, Numerical analysis of circular graphene bubbles, *J. Appl. Mech.* **80**, 040905 (2013).
- ¹⁶ See Supplemental Material at <http://link.aps.org/supplemental/>... for detailed description of theoretical modelling, evaluation of strain and comparison with literature, micro-Raman experiments, effect of dome capping on the dome volume vs T, funneling effect details, and results found in other 2D TMDs.

-
- ¹⁷. W. B. Fichter, Some solutions for the large deflections of uniformly loaded circular membranes, NASA Technical Paper **3658**, 1 (1997).
- ¹⁸. P. Johari and V. B. Shenoy, Tuning the electronic properties of semiconducting transition metal dichalcogenides by applying mechanical strains. ACS Nano **6**, 5449 (2012).
- ¹⁹ S. Horzum, H. Sahin, S. Cahangirov, P. Cudazzo, A. Rubio, T. Serin, and F. M. Peeters, Phonon softening and direct to indirect band gap crossover in strained single-layer MoSe₂, Phys. Rev. B **87**, 125415 (2013).
- ²⁰. M. Ghorbani-Asl, S. Borini, A. Kuc, and T. Heine, Strain-dependent modulation on conductivity in single-layer transition-metal dichalcogenides. Phys. Rev. B **87**, 235434 (2013).
- ²¹. H. Shi, H. Pan, Y.-W. Zhang, and B. I. Yakobson, Quasiparticle band structures and optical properties of strained monolayer MoS₂ and WS₂. Phys. Rev. B **87**, 155304 (2013).
- ²². C.-H. Chang, X. Fan, S.-H. Lin, and J.-L. Kuo, Orbital analysis of electronic structure and phonon dispersion in MoS₂, MoSe₂, WS₂, and WSe₂ monolayers under strain. Phys. Rev. B **88**, 195410 (2013).
- ²³ B. Amin, T. P. Kaloni, and U. Schwingenschl, Strain engineering of WS₂, WSe₂, and WTe₂, RCS Adv. **4**, 34561 (2014).
- ²⁴. Das, R., Rakshit, B., Debnath, S., & Mahadevan, P. Microscopic model for the strain-driven direct to indirect band-gap transition in monolayer MoS₂ and ZnO. Phys. Rev. B **89**, 115201 (2014).
- ²⁵. L. Ortenzi, L. Pietronero, and E. Cappelluti, Zero-point motion and direct-indirect band-gap crossover in layered transition-metal dichalcogenides, Phys. Rev. B **98**, 195313 (2018).

-
- ²⁶. F. Wang, I. A. Kinloch, D. Wolverson, R. Tenne, A. Zak, E. O'Connell, U. Bangert, and R. J. Young, Strain-induced phonon shifts in tungsten disulphide nanoplatelets and nanotubes, *2D Materials* **4**, 015007 (2017).
- ²⁷. A. M. Dadgar, D. Scullion, K. Kang, D. Esposito, E.-H. Yang, I. P. Herman, M. A. Pimenta, E.-J. G. Santos, and A. N. Pasupathy, Achieving large, tunable strain in monolayer transition-metal dichalcogenides, *Chem. Mater.* **30**, 5148 (2018).
- ²⁸ Q. Zhang, Z. Chang, G. Xu, Z. Wang, Y. Zhang, Z.-Q. Xu, S. Chen, Q. Bao, J. Z. Liu, Y.-W. Mai, W. Duan, M. S. Fuhrer, and C. Zheng, Strain Relaxation of Monolayer WS₂ on Plastic Substrate, *Adv. Funct. Mater.* **26**, 8707-8714 (2016).
- ²⁹ R. Yang, J. Lee, S. Ghosh, H. Tang, R. M. Sankaran, C. A. Zorman, and P. X.-L. Feng, Tuning optical signatures of single- and few-layer MoS₂ by blown-bubble bulge straining up to fracture, *Nano Lett.* **17**, 4568 (2017).
- ³⁰. R. Frisenda, M. Drüppel, R. Schmidt, S. M. de Vasconcellos, D. P. de Lara, R. Bratschitsch, M. Rohlfing, and A. Castellanos-Gomez, Biaxial strain tuning of the optical properties of single-layer transition metal dichalcogenides. *2D Materials* **4**, 10 (2017).
- ³¹. H. J. Conley, B. Wang, J. I. Ziegler, R. F. Haglund Jr., S. T. Pantelides, and K. I. Bolotin, Bandgap engineering of strained monolayer and bilayer MoS₂. *Nano Lett.* **13**, 3626 (2013).
- ³² J. Chaste, A. Missaoui, S. Huang, H. Henck, Z. Ben Aziza, L. Ferlazzo, C. Naylor, A. Balan, A. T. C. Johnson Jr., R. Braive, and A. Ouerghi, Intrinsic Properties of Suspended MoS₂ on SiO₂/Si Pillar Arrays for Nanomechanics and Optics, *ACS Nano* **12**, 3235-3242 (2018).
- ³³. Y. Wang, C. Cong, W. Yang, J. Shang, N. Peimyoo, Y. Chen, J. Kang, J. Wang, W. Huang, and T. Yu, Strain-induced direct-indirect bandgap transition and phonon modulation in monolayer WS₂. *Nano Res.* **8**, 2562 (2015).

-
- ³⁴ C. Robert, D. Lagarde, F. Cadiz, G. Wang, B. Lassagne, T. Amand, A. Balocchi, P. Renucci, S. Tongay, B. Urbaszek, and X. Marie., Exciton radiative lifetime in transition metal dichalcogenide monolayers, *Phys. Rev. B* **93**, 205423 (2016).
- ³⁵ H. Liu, T. Wang, C. Wang, D. Liu and J. Luo, Exciton Radiative Recombination Dynamics and Nonradiative Energy Transfer in Two-Dimensional Transition-Metal Dichalcogenides, *J. Phys. Chem. C* **123**, 10087 (2019).
- ³⁶ J. J. Esteve-Paredes, S. Pakdel, and J. J. Palacios, Quenching of Exciton Recombination un Strained Two-Dimensional Monochalcogenides, *Phys. Rev. Lett.* **123**, 077402 (2019).
- ³⁷ Y. Sun, S. E. Thompson, T. Nishida, *Strain Effect in Semiconductors: Theory and Device Applications*, Springer, New York, Ch. 2 (2010).
- ³⁸ X. He, H. Li, Z. Zhu, Z. Dai, Y. Yang, P. Yang, Q. Zhang, P. Li, U. Schwingenschlogl, and X. Zhang, Strain engineering in monolayer WS₂, MoS₂, and the WS₂/MoS₂ heterostructure, *Appl. Phys. Lett.* **109**, 173105 (2016).
- ³⁹ Z. Jin, X. Li, J. T. Mullen, and K. W. Kim, Intrinsic transport properties of electrons and holes in monolayer transition-metal dichalcogenides, *Phys. Rev. B* **90**, 045422 (2014).

Supplemental Material for

Variation of the fundamental band gap nature in curved two-dimensional WS₂

E. Blundo[‡], M. Felici[‡], T. Yildirim[†], G. Pettinari[◇], D. Tedeschi[‡], A. Miriametro[‡], B. Liu[†], W. Ma[†], Y.

Lu,^{†#} and A. Polimeni^{‡,}*

[‡] Dipartimento di Fisica, Sapienza Università di Roma, 00185 Roma, Italy

[†] Research School of Electrical, Energy and Materials Engineering, College of Engineering and

Computer Science, The Australian National University, Canberra, ACT 2601, Australia

[◇] Institute for Photonics and Nanotechnologies, National Research Council, 00156 Roma, Italy

[#] ARC Centre of Excellence in Future Low-Energy Electronics Technologies (FLEET) ANU node,

Canberra, ACT 2601, Australia

* antonio.polimeni@roma1.infn.it

Abstract

In this Supplemental Material we (i) provide details about the finite-element method employed to calculate the strain tensor over spherically-deformed WS₂ membranes or domes, (ii) evaluate the biaxial strain acting on the domes' summit according to a continuum mechanical model, (iii) show micro-Raman measurements over the dome surface to account for the strain gradient, (iv) report the effect of methylpentane capping on the temperature dependence of the dome volume, (v) explain how the funneling effect was taken into account to determine the Γ -K cross-over in the valence band, (vi) show results about the direct-to-indirect band gap transition in MoS₂ and WSe₂.

Contents

1. FEM profile and strain modelling	1
2. Evaluation of biaxial strain at the dome summit (Hencky's model)	6
3. Micro-Raman measurements	8
4. Effects of methylpentane deposition on the T dependence of the dome's size	10
5. Direct-to-indirect band gap transition and funneling effect	12
6. Direct-to-indirect band gap transition in MoS ₂ and WSe ₂ monolayers	14
References	16

1. FEM profile and strain modelling

The height profile of the domes and the evolution of the strain tensor across the domes' surface were modelled via finite-element method (FEM) calculations in the framework of nonlinear-membrane theory were employed.¹ The presence of hydrogen gas within the domes following proton irradiation is modelled as an internal, upward pressure load acting on the flat membrane surface. To run the calculations, the radius of the dome, the pressure of the hydrogen gas and the elasticity matrix (as accounted for below) of the compound are given as input parameters to simulate the interplay between adhesion forces, gas expansion and elastic forces. The pressure value is chosen so that the simulated dome maximum height matches that one measured by AFM. The relatively small size of the domes allows us to use membrane theory and to neglect the effects of bending stiffness. Moreover, due to the relatively large dome heights compared to the thickness of a MX₂ monolayer (ML), we employ a nonlinear Green-Lagrange strain tensor. Thanks to the mirrored symmetry about the longitudinal axis of the domes, an axisymmetric formulation using polar coordinates is used. Thus, a model implemented in COMSOL Multiphysics 5.1 is employed for the simulations of the dome formation. A line element is used to simulate the membrane with the starting thickness of a MX₂ ML. One end of the line element is subjected to a fixed constraint (*i.e.* null displacement) while the rest of the line is free to move in the longitudinal direction. An extra fine mesh is used for all simulations and a 0.001 convergence setting is used to ensure the numerical accuracy of the solutions. A constant Newtonian solver is used for the numerical solver procedure. Due to the anisotropic stiffness of MX₂ compounds, an anisotropic stiffness matrix was implemented in the linear elastic material node^{2,3,4}.

The following anisotropic elasticity matrices^{2,3} (all units in GPa) were here employed.

For MoS₂,

$$D = \begin{pmatrix} 178 & 45 & 1 & 0 & 0 & 0 \\ 45 & 178 & 1 & 0 & 0 & 0 \\ 1 & 1 & 3 & 0 & 0 & 0 \\ 0 & 0 & 0 & 1 & 0 & 0 \\ 0 & 0 & 0 & 0 & 1 & 0 \\ 0 & 0 & 0 & 0 & 0 & 67 \end{pmatrix}$$

For WSe₂,

$$D = \begin{pmatrix} 158 & 31 & 1 & 0 & 0 & 0 \\ 31 & 158 & 1 & 0 & 0 & 0 \\ 1 & 1 & 2 & 0 & 0 & 0 \\ 0 & 0 & 0 & 1 & 0 & 0 \\ 0 & 0 & 0 & 0 & 1 & 0 \\ 0 & 0 & 0 & 0 & 0 & 64 \end{pmatrix}$$

In the case of WS₂, only the matrix elements D₁₂, D₂₂, and D₆₆ could be found in Refs. 2, 3 and 5. However, the other elements are almost the same for all the compounds. Due to the analogous effect induced by strain on the lattice constant⁶, for the unknown elements the same elements of the MoS₂ matrix were used, so that the following anisotropic elasticity matrix was used for the WS₂ simulations.

$$D = \begin{pmatrix} 196 & 43 & 1 & 0 & 0 & 0 \\ 43 & 196 & 1 & 0 & 0 & 0 \\ 1 & 1 & 3 & 0 & 0 & 0 \\ 0 & 0 & 0 & 1 & 0 & 0 \\ 0 & 0 & 0 & 0 & 1 & 0 \\ 0 & 0 & 0 & 0 & 0 & 76 \end{pmatrix}$$

We point out that the Poisson's ratios calculated from the values reported in these matrices ($\nu=D_{12}/D_{22}$) are in excellent agreement with the values reported in other works (see Supplementary Note 2).

The mechanical model here described allows us to reproduce the dome shape and calculate the principal components of the strain tensor, as displayed in Fig. S1 for WS₂, MoS₂, and WSe₂. The use of the principal components ensures that the strain tensor is a diagonal matrix, i.e., there are no shear-strain components to take into account. A sketch of the three principal components is given in Fig. 2a of the main text. The tensor is characterized by two in-plane components: The circumferential (ε_t) and radial (ε_r) components -analogously defined to Ref. 1- and by an out-of-plane component: The perpendicular strain component (ε_z). Moreover, for biaxially strained TMDs, the perpendicular component of the strain tensor can be written as⁷ $\varepsilon_z = -\frac{D_{13}}{D_{33}}(\varepsilon_r + \varepsilon_t)$, where D_{13} and D_{33} are the pertinent elements of the elasticity matrix reported above. Notice that this implies that $\varepsilon_z < 0$, accounting for a compression in the out-of-plane direction that increases as $(\varepsilon_r + \varepsilon_t)$ increases.

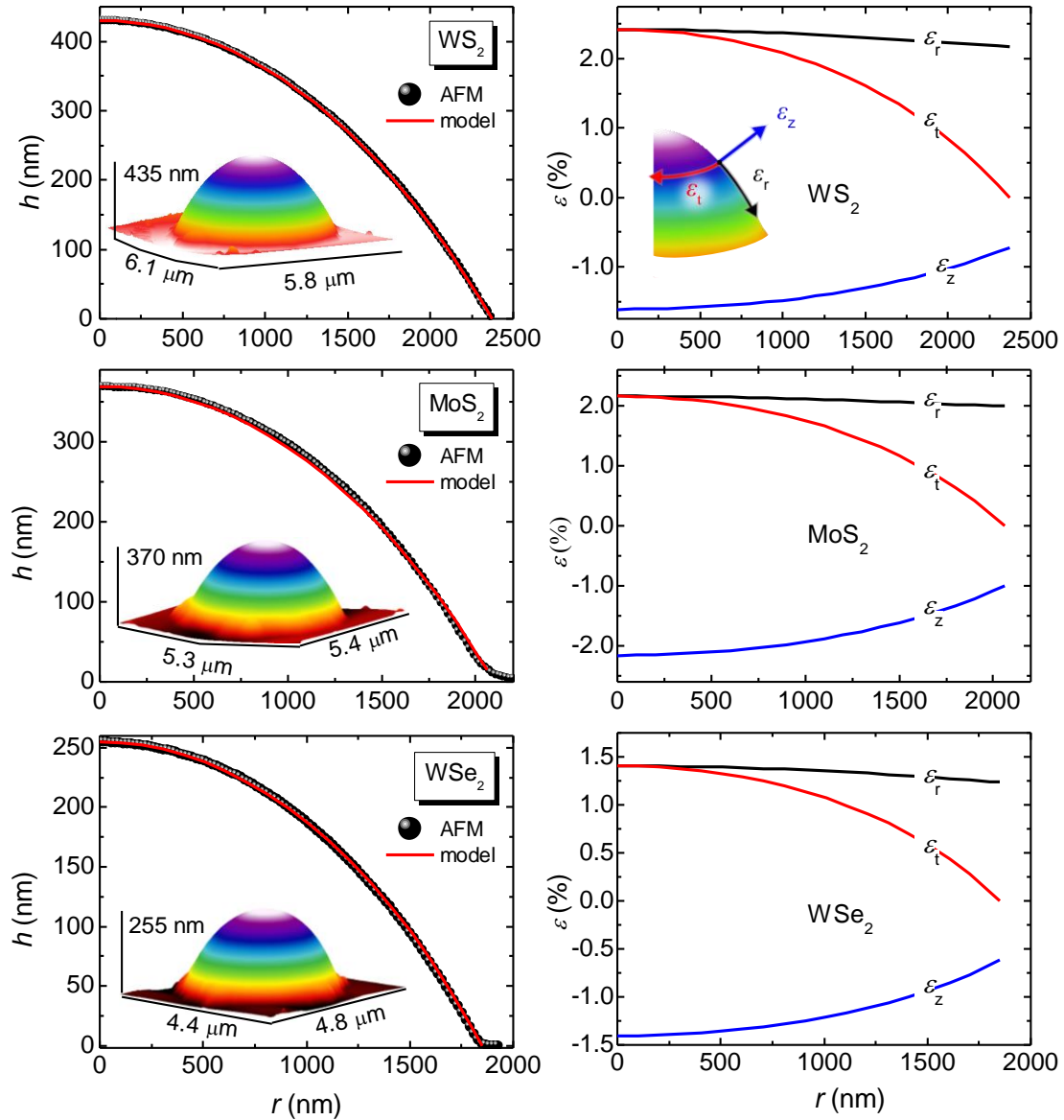


Figure S1. Mechanical model vs experiment.

Left panels: Experimental dependence of the dome height h on the radial coordinate r (points) for domes formed by different TMD materials. The h - r plots were derived from the atomic force microscope images shown as insets. The red lines are the results of the mechanical model employed to reproduce the dome shape and calculate the strain tensor components displayed on the right panels. **Right panels:** Dependence of the principal components of the strain tensor on the radial coordinate r of the domes. The definition of the radial (ϵ_r) and circumferential (ϵ_t) in-plane components and of the perpendicular (ϵ_z) out-of-plane strain component are depicted in the inset of the first panel on the right.

The results obtained by means of this mechanical model for the strain tensor are in good agreement with Hencky's model (described in the next paragraph). In Table 1 we report a comparison between Hencky's model and our model, for the 3 domes of Fig. S1.

	Hencky's model ^{8,9}	this work
WS ₂	2.40%	2.43%
MoS ₂	2.13%	2.16%
WSe ₂	1.40%	1.40%

Table 1: Comparison between the expected values of the strain at the dome summit evaluated by Hencky's model^{8,9} $\varepsilon_m = \varepsilon_t = \varepsilon_r = f(\nu) \cdot (h_m/R)^2$ (see Supplementary Note 2) and those derived by our mechanical model. The values reported in the table refer to the domes whose data are shown in Figure S1.

Besides the height and strain profile, the mechanical model here described also allows us to estimate the internal pressure of the gas contained within the domes. The estimation of the pressure dependence on the dome footprint radius is displayed in Fig. S2 for WS₂ domes.

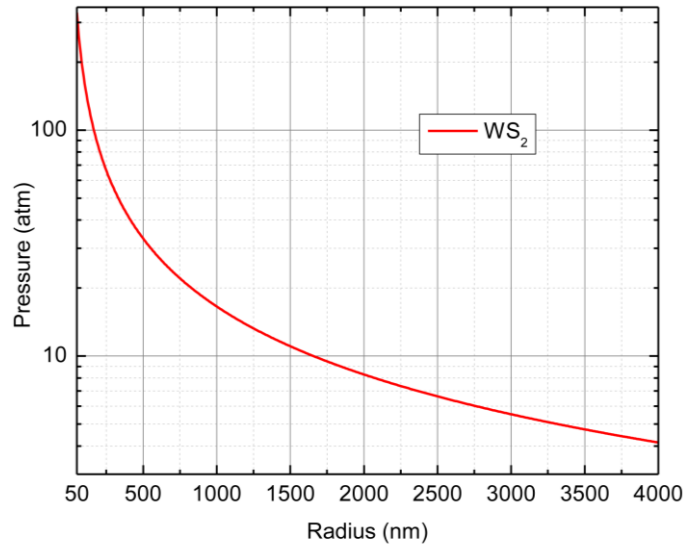


Figure S2. Internal pressure estimation.

Predicted dependence of the H₂ pressure as a function of the dome footprint radius in WS₂ domes. The data are evaluated by using the same mechanical model employed for simulating the dome profile and determining the strain tensor components.

2. Evaluation of biaxial strain at the dome summit (Hencky's model)

The expression for biaxial strain at the top of the dome is accounted for in Refs. 8 and 9 and is given by the Hencky's formula:

$$\varepsilon_m = \left(\frac{h_m}{R}\right)^2 f(\nu) = \left(\frac{h_m}{R}\right)^2 \frac{b_0(\nu)(1-\nu)K(\nu)^{2/3}}{4},$$

where h_m and R are the maximum height and the footprint radius of the dome, respectively. b_0 and K are two quantities that depend only on the Poisson's ratio ν . The values of ν for all the materials illustrated in Fig. S1 are listed in the following table¹⁰.

	WS ₂	MoS ₂	WSe ₂
ν	0.217	0.249	0.192

Table 1. Poisson's ratios.

Poisson's ratios for the six compounds (after Ref. 10).

b_0 and K can be evaluated by numerical methods. Therefore, to estimate them we perform an interpolation between the values reported in the literature^{9,11} from which we finally get $f(\nu)$ for all the compounds shown in Fig. S1. The values of b_0 , K , and $f(\nu)$ employed in this work are listed in the following table.

	WS ₂	MoS ₂	WSe ₂
b_0	1.689	1.702	1.680
K	3.274	3.386	3.192
$f(\nu)$	0.729	0.721	0.736

Table 2. b_0 , K , and $f(\nu)$.

Values of b_0 , K , and $f(\nu)$ calculated via an interpolation between the values reported in the literature^{9,11}.

Finally, the average values of the h_m/R ratio and of ε_m —as obtained from the analysis of the data presented in Fig. S1—are reported in the following table for all the compounds investigated here:

	WS ₂	MoS ₂	WSe ₂
h_m/R	0.16±0.02	0.16±0.02	0.15±0.01
ε_m	(2.0±0.4)%	(1.8±0.4)%	(1.6±0.2)%

Table 3. Aspect ratios and strain at the summit.

First row: Average values of the aspect ratios (h_m/R) for the three compounds.

Second row: Average values for the strain at the summit, calculated for the three compounds according to Hencky's formula and using the aspect ratios in the first row and the values of $f(v)$ reported in Table 2.

3. Micro-Raman measurements

The following figure shows a micro-Raman mapping performed along the diameter of the same WS₂ dome, whose micro-PL mapping is shown and discussed in Fig. 2 of the main text. Details about micro-Raman measurements are reported in the caption of following Figure S3.

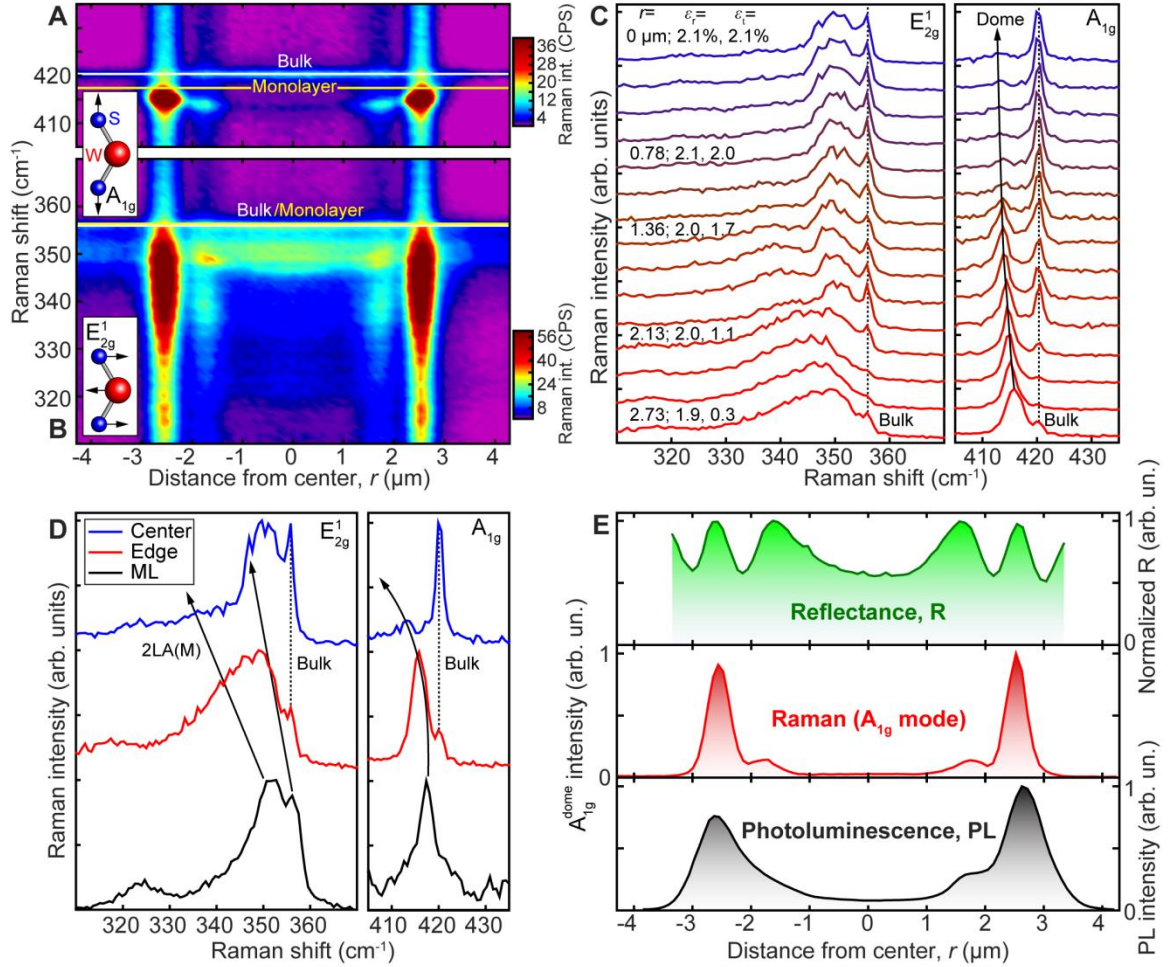


Figure S3. μ -Raman mapping of a WS₂ dome

(A) One-dimensional, room-temperature ($T = 297$ K) micro-Raman scan across a WS₂ dome, in the spectral region of the A_{1g} phonon mode (the dome is the same one displayed in Fig. 2a of the main text). The horizontal axis indicates the laser spot position with respect to the dome center (r), whereas the vertical axis indicates the Raman shift with respect to the laser line (laser wavelength $\lambda = 532.2$ nm). The micro-Raman intensity is shown in a false color scale (see colorbar). The white (yellow) line marks the position of the A_{1g} mode in bulk (monolayer) WS₂^{12,13}. **Inset:** Atomic displacements associated with the A_{1g} mode (the vertical axis of the sketch is perpendicular to the monolayer plane). (B) Same as Panel A, but for the E_{2g}¹ mode. (C) **Left:** Evolution of the normalized micro-Raman spectrum of the dome ($T = 297$ K) in the spectral region of the E_{2g}¹ mode,

as the laser spot is scanned from the dome's right edge (bottom) to its apex (top). Some selected spectra are labeled with the position of the laser spot and with the values of the radial (ε_r) and circumferential (ε_t) components of the strain tensor (see Fig. 2a of the main text and Supplementary Fig. S1). The dotted line marks the position of the E_{2g}^1 mode in bulk WS_2 . **Right:** Same as on the left, but for the A_{1g} mode. The black arrow follows the mode shift as the laser is scanned across the dome. **(D) Right:** Comparison between the normalized micro-Raman spectrum ($T = 297$ K) in monolayer WS_2 (bottom) and at the edge (middle) and in the center (top) of the dome, in the spectral region of the E_{2g}^1 mode. The dotted line marks the position of the E_{2g}^1 mode in bulk WS_2 ; the arrows follow the Raman shifts of the E_{2g}^1 and 2LA(M) modes. The mode at 330 cm^{-1} in the ML spectrum was also observed in Ref. 14. We tentatively ascribe this mode to a LA replica. **Right:** Same as on the left, but for the A_{1g} mode. **(E) Bottom:** Dependence of the integrated micro-PL intensity on the position of the laser spot. In order to obtain the displayed intensity profile, the micro-PL spectra displayed in panels b-c of Fig. 3a in the main text were integrated between 1.7 and 1.95 eV. **Middle:** Evolution of the intensity of the A_{1g} Raman mode as the laser is scanned across the dome. The reported intensity values were obtained by fitting each Raman spectrum (see panel A and the right-hand side of panel C) with the function $I_{\text{tot}} = I_{\text{dome}} + I_{\text{bulk}} + I_{\text{bkg}}$. Here, I_{tot} is the total spectrum, whereas I_{bkg} is a flat background. I_{dome} and I_{bulk} are Gaussian functions, respectively taking into account the Raman peaks associated with lattice vibrations in the dome layer and in the underlying bulk WS_2 . In the panel we report $I_{\text{dome}} + I_{\text{bkg}}$, thereby excluding the contribution of bulk WS_2 to the spectrum. **Top:** Normalized reflectance at 532.2 nm as a function of the position of the laser spot. The displayed profile was obtained by collecting the light reflected by the sample as the laser was scanned across the dome, under the same experimental conditions used for micro-Raman and micro-PL measurements (laser wavelength $\lambda = 532.2$ nm, $T = 300$ K, confocal configuration). Note the much different dynamic range spanned by the three intensity profiles with a ratio between the maximal and minimal value equal to 13 and 33 for the micro-PL and micro-Raman profiles, respectively. For micro-PL it is straightforward to ascribe this intensity reduction to the direct-to-indirect band gap transition taking place as one moves from the edge to the center of the dome (see main text, Fig. 2). An analogous behavior to that of the dome discussed in Fig. 2b,c is found also for other WS_2 domes despite of their different dimensions, as also attested by the same ring-like pattern of the laser-excited red luminescence observed for all the domes in Fig. 1c, which suggests a minor role to be played by interference. It seems reasonable to assume a similar origin for the observed reduction of the micro-Raman signal at the dome's center. In this case, some interferential effects can be noticed in between the edge and the center of the dome, where an analogous modulation to that of the reflectance profile can be seen (see, in particular, the minimum for $r \sim \pm 2\ \mu\text{m}$). We can therefore conclude that the modulation of the micro-PL and micro-Raman profiles are chiefly due to the strain-induced variations of the electronic properties across the surface of our domes, and interference does not play a primary role.

4. Effects of methylpentane deposition on the T dependence of the dome's size

As reported in Ref. 15, the contraction of the H_2 gas trapped inside a dome leads to a progressive reduction of the dome's volume at cryogenic temperatures, which culminates in the dome's disappearance upon reaching the vapor-to-liquid transition temperature at about 32 K. Even though this phenomenon is fully reversible (each dome reappears in its original position when the temperature is increased), the dome's shrinkage at cryogenic temperatures makes it increasingly difficult to spatially resolve the micro-PL signal from different zones of the dome. As noted in the main text, this is potentially highly problematic for time-resolved micro-PL measurements, which must be performed at low temperature to fully appreciate the existing differences in the temporal behavior of the direct and indirect exciton. At room temperature, indeed, non-radiative decay channels dominate the exciton dynamics, as also reported, *e.g.*, in Ref. 16. As illustrated in Fig. S4, however, this issue can be conveniently overcome by covering the sample surface with a thin layer of methylpentane. Indeed, the adhesion of the latter to the dome's walls is enough to nearly stop the dome's contraction with decreasing T , without sizably altering the dome's emission properties (see main text).

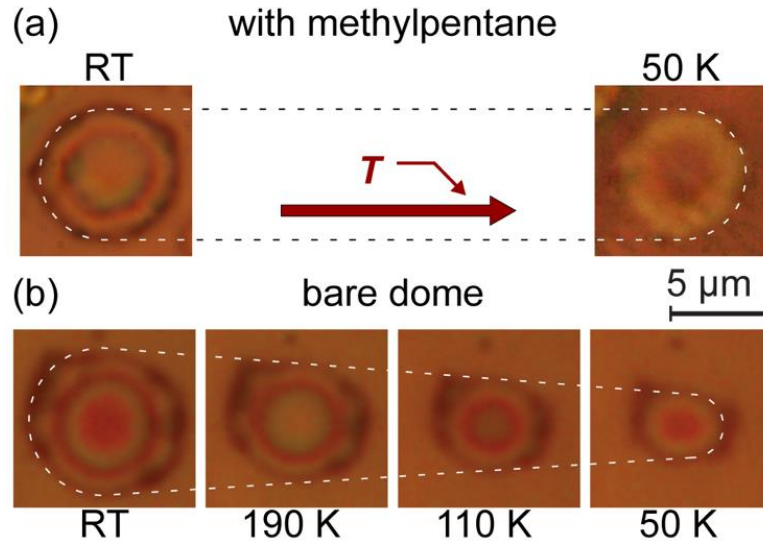


Figure S4. Slowing down the dome’s contraction at low T by methylpentane deposition

(a) Optical microscope images of the WS₂ dome on which the time-resolved micro-PL measurements discussed in the main text (see Fig. 3) were acquired. The image on the left was acquired at room temperature ($T \sim 290$ K), whereas the image on the right was taken at $T = 50$ K (*i.e.*, the temperature at which the time-resolved micro-PL measurements were performed). Even though the same $100\times$ objective ($NA = 0.75$) was used for both images, the quality of the one acquired at $T = 50$ K is affected by the aberrations due to the presence of the optical cryostat window in between the objective and the sample. Nevertheless, the effects of methylpentane deposition are clearly visible, *i.e.*, the dome’s size becomes nearly insensitive to temperature changes. This is in sharp contrast with the situation depicted in panel (b), which displays the T dependence of the dome’s size in a “bare” (*i.e.*, not covered with methylpentane) sample. The dome’s shrinkage with decreasing T is clearly visible in the displayed optical images (acquired with a $50\times$ objective with $NA = 0.5$).

5. Direct-to-indirect band gap transition and funneling effect

First of all, we justify Eq. (1) of the main text, according to which

$$E_{A,I}(\varepsilon_p) = E_{A,I}(0) - \Delta_{A,I} \cdot \varepsilon_p. \quad (\text{S1})$$

In particular, we need to clarify why the energies of the A and I excitons only depend on the total in-plane strain, $\varepsilon_p = \varepsilon_r + \varepsilon_t$, rather than being an explicit function of the three principal components of the strain tensor, namely

$$E_{A,I}(\varepsilon_r, \varepsilon_t, \varepsilon_z) = E_{A,I}(0) - (\Delta_{A,I}^r \cdot \varepsilon_r + \Delta_{A,I}^t \cdot \varepsilon_t + \Delta_{A,I}^z \cdot \varepsilon_z) \quad (\text{S2})$$

(it should be noted that the use of the principal components implies that the strain tensor is a diagonal matrix, *i.e.*, there are no shear-strain components to be taken into account). According to Ref. 6, the energy shifts of the first Brillouin-zone critical points of TMD MLs induced by the presence of an in-plane uniaxial tensile strain do not depend heavily on the direction along which the deformation is exerted, so that we can write $\Delta_{A,I}^r \cdot \varepsilon_r + \Delta_{A,I}^t \cdot \varepsilon_t \sim \Delta_{A,I}^p \cdot (\varepsilon_r + \varepsilon_t) = \Delta_{A,I}^p \cdot \varepsilon_p$. Moreover, as we noted in the main text, for biaxially strained TMDs the perpendicular component of the strain tensor can be written as $\varepsilon_z = -\frac{D_{13}}{D_{33}}\varepsilon_p$, where D_{13} and D_{33} are the pertinent components of the elasticity matrix reported in Section 1 of this supplemental Material¹⁷. As a consequence, Eq. (S2) can be rewritten as

$$E_{A,I}(\varepsilon_p) = E_{A,I}(0) - \left(\Delta_{A,I}^p \cdot \varepsilon_p - \Delta_{A,I}^z \cdot \frac{D_{13}}{D_{33}} \varepsilon_p \right), \quad (\text{S3})$$

which is identical to Eq. (S1) (*i.e.*, to Eq. (1) of the main text), with $\Delta_{A,I} = \Delta_{A,I}^p - \Delta_{A,I}^z \cdot \frac{D_{13}}{D_{33}}$. The validity of Eq. (1) of the main text implies that the analysis of the dependence of $E_{A,I}$ on ε_p can yield important information on the energy bands of WS_2 —such as the energy of the I exciton for zero strain, $E_I(0)$ —and on their dependence on strain, quantified through the $\Delta_{A,I}$ energy shift rates. In order to extract this information from the experimental data reported in Fig. 4 of the main text, however, we have to take into account the continuous reduction of the energy gap of the material on going from the edge to the center of the curved dome's surface. As a consequence of this reduction,

the photogenerated carriers drift towards the minimum energy available within their diffusion length (funnel effect)^{18,19}, *i.e.*, towards the dome's center. Combined with the finite exciting/collecting area of the objective, this alters profoundly the correspondence between the coordinate r (and thus ε_p) and the exciton energy resulting from the emission spectra. The curves superimposed on the experimental data in Fig. 4 simulate the local values of the energies of the A and I exciton band gaps. These latter were deduced by a model in which exciton annihilation takes place in the minimum energy available within the objective collection area¹⁹. For each set of data, the solid line results from a fit performed by fixing the radius of the collection area, R_c , to 2.5σ ($\sigma = 0.23 \mu\text{m}$ is the laser spot size; see Ref. 12 in the main text), whereas the shaded areas are delimited by the fitting curves (barely observable) obtained for $R_c = 2\sigma$ and 3σ . This range of R_c —which ultimately sets the uncertainty of our fitting procedure—was chosen to account for the effect of the pinhole used to spatially filter the collected light in our confocal microscope, which was indeed verified to transmit between 95% and 99% of the laser light reflected by the sample. The actual (*i.e.*, free from the funnel effect) strain dependences of the A and I excitons are provided in Fig. 4b by blue and red dashed lines—again computed for $R_c = 2.5\sigma$ —and by their corresponding shaded areas, indicating the regions spanned by the theoretical trends in the $2\sigma \leq R_c \leq 3\sigma$ range.

	Our work	Literature
Δ_A (meV/%)	45	46^{20} , 47^{21}
Δ_I (meV/%)	$2.0 \Delta_A$	$1.1 \cdot \Delta_A^{22}$, $2.1 \cdot \Delta_A^{23}$
$E_I(0) - E_A(0)$ (meV)	130	117^{22} , 125^{23} , 173^{24}
$\varepsilon_{\text{transition}}$ (%)	2.7	$\geq 2^{6,25,26}$

Table 1. comparison with literature.

Shift rate values Δ of the direct (A) and indirect (I) exciton energy. $E_{A,I}(0)$ indicates the direct and indirect exciton energies at zero strain. In order to make meaningful a comparison with theoretical papers (where the absolute value of the band gap is underestimated), we report the difference between these quantities.

6. Direct-to-indirect band gap transition in MoS₂ and WSe₂ monolayers

The findings reported for WS₂ are general and were observed also in other TMD compounds. In the following figure S5, we show the micro-PL spectra recorded in different points of a single MoS₂ (left) and WSe₂ (right) dome, showing the dramatic changes of the emission spectrum on going from the dome's edge to its center.

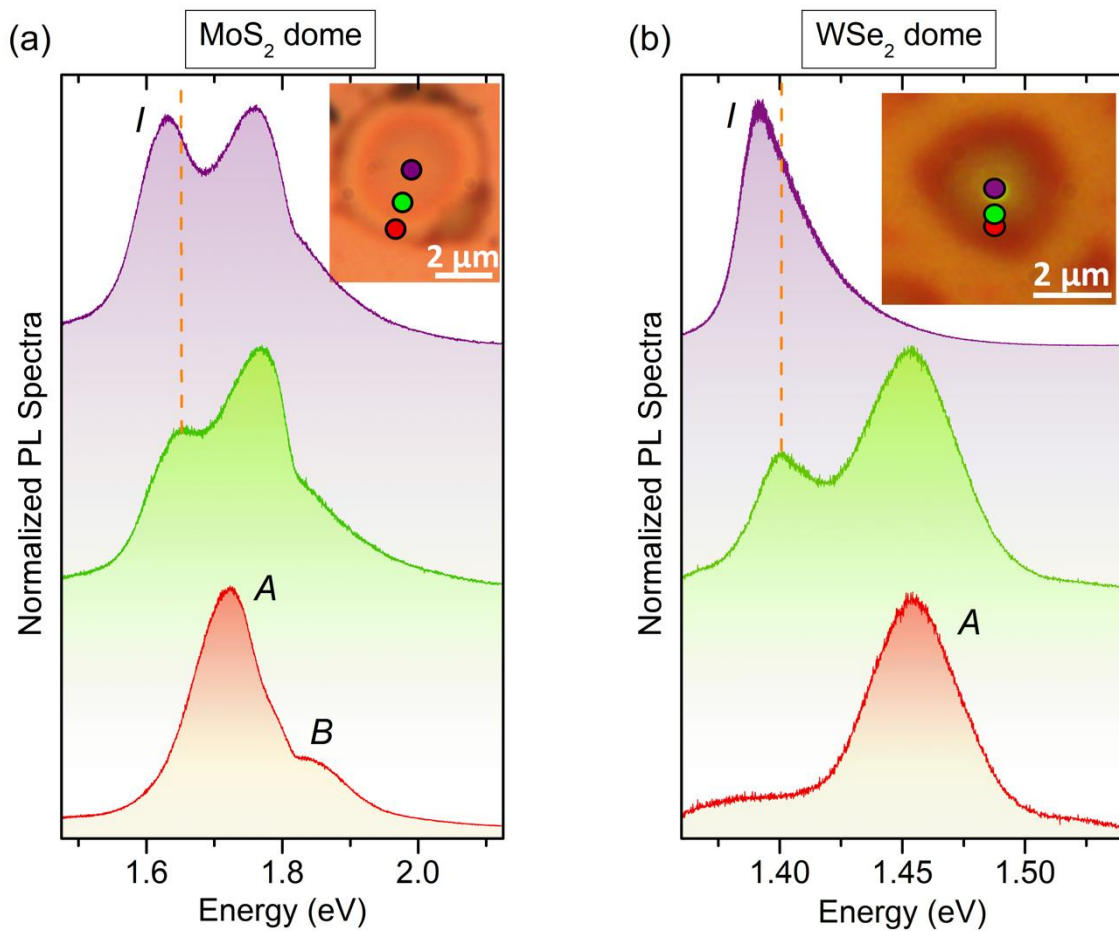


Figure S5. Direct-to-indirect bandgap crossover in MoS₂ and WSe₂ domes.

(a) micro-PL spectra acquired in the positions highlighted by the colored dots in the MoS₂ dome (with footprint radius $R = (2.46 \pm 0.06) \mu\text{m}$) shown as inset. The spectra are peak-normalized for ease of comparison. At the edges of the dome (red dot in the inset) the direct *A* exciton (corresponding to the K_C - K_V transition) dominates the spectrum (red spectrum) and the *B* exciton involving the conduction band minimum at K_C and the lower split band at K_V in valence band can also be observed. According to our mechanical model, at the edges of MoS₂ domes the strain is strongly anisotropic with a radial component equal to $\sim 2\%$ and an almost null circumferential component (see Supplementary Figure S1). The *A* peak appears to be broad and composite due to the complex strain distribution coupled to the finite resolution of our optical system (as discussed in

the main text) and to funneling phenomena. These factors are also likely responsible for irregular behaviors close to the edges, such as the unexpected blueshift (of ~ 30 meV) observed while moving towards the dome center (green dot in the inset and corresponding green spectrum). Notice that deviations from the expected behavior towards higher energies were similarly observed also for uniaxially-strained MoS₂ monolayers in Ref. 27, for strains $\gtrsim 1.4$ %. The *A* band then redshifts while further going towards the center, where strain features a more regular biaxial distribution with $\varepsilon_r \approx \varepsilon_t$. In between the edges and the center (see green dot in the inset and corresponding green spectrum) a new band (*I*) appears, which we attribute to the indirect K_C- Γ _V transition. This band starts dominating the spectrum at the dome summit (purple dot in the inset and corresponding purple spectrum). Notice that at the center the *I* and *A* band are redshifted by about 20 meV and 10 meV, respectively, with respect to the green dot, accordingly to the increase of biaxial strain and the theoretically predicted higher shift rate for the K_C- Γ _V transition with respect to the K_C-K_V transition^{22,23}. The dashed orange line highlights the redshift of the *I* exciton. Concomitantly, a reduction in the PL signal is observed, the PL signal at the edge being ~ 10 times more intense than at the center. Based on our μ -PL measurements on several MoS₂ domes, the bandgap crossover is found to occur for this compound for an in-plane strain ~ 3 -4 %. **(b)** Same as in panel (a) for the WSe₂ dome (with footprint radius $R = (1.42 \pm 0.06)$ μm) shown as inset. The direct *A* exciton (corresponding to the K_C-K_V transition) dominates the spectrum at the edges (red dot in the inset and corresponding red spectrum). The indirect *I* band appears while moving towards the center (green dot and corresponding green spectrum), redshifts while approaching the dome summit (as highlighted by the dashed orange line) and finally dominates the spectrum (purple dot and spectrum). For this compound, no significant quenching of the PL signal is observed for increasing tensile strain, the signal often increasing while going from the edges towards the domes' summit. An increase in the PL emission was also observed in Ref. 28 for WSe₂ monolayer under uniaxial strain. In our domes, however, the signal is observed not to decrease even in presence of the direct-to-indirect bandgap transition (for the dome here shown the signal at the center is found to be almost 10 times higher than at the edges). This enhancement in the PL efficiency is likely aided by funneling effects combined with the small dimensions of the WSe₂ domes we can create: The larger domes have dimensions comparable to that of the excitation laser spot, resulting in funneling of excitons at the dome summit and thus favoring the indirect transition. For WSe₂, the bandgap crossover is found to occur for an in-plane strain ~ 2 -3 %.

References

- ¹ P. Wang, W. Gao, Z. Cao, K. M. Liechti, and R. Huang, Numerical Analysis of Circular Graphene Bubbles, *J. Appl. Mech.* **80**, 040906 (2013).
- ² A. Jain, S. P. Ong, G. Hautier, W. Chen, W. D. Richards, S. Dacek, S. Cholia, D. Gunter, D. Skinner, G. Ceder, and K. A. Persson, Commentary: The Materials Project: A materials genome approach to accelerating materials innovation, *APL Mater.* **1**, 011002 (2013).
- ³ M. de Jong, W. Chen, T. Angsten, A. Jain, R. Notestine, A. Gamst, M. Sluiter, C. K. Ande, S. van der Zwaag, J. J. Plata, C. Toher, S. Curtarolo, G. Ceder, K. A. Persson, and M. Asta, Charting the complete elastic properties of inorganic crystalline compounds, *Sci. Data* **2**, 150009 (2015).
- ⁴ The Materials Project, <https://materialsproject.org/> (2018).
- ⁵ M. M. Alyörük, Y. Aierken, D. Çakır, F. M. Peeters, and C. Sevik, Promising piezoelectric performance of single layer transition-metal dichalcogenides and dioxides, *J. Phys. Chem. C* **119**, 23231-23237 (2015).
- ⁶ P. Johari and V. B. Shenoy, Tuning the electronic properties of semiconducting transition metal dichalcogenides by applying mechanical strains, *ACS Nano* **6**, 5449 (2012).
- ⁷ Y. Sun, S. E. Thompson, and T. Nishida, *Strain Effect in Semiconductors: Theory and Device Applications*, Springer, New York, Ch. 2, 2010.
- ⁸ W. B. Fichter, Some solutions for the large deflections of uniformly loaded circular membranes, *NASA Tech. Pap.* **3658**, 1 (1997).
- ⁹ D. Lloyd, X. Liu, J. W. Christopher, L. Cantley, A. Wadehra, B. L. Kim, B. B. Goldberg, A. K. Swan, and J. S. Bunch, Band gap engineering with ultralarge biaxial strains in suspended monolayer MoS₂, *Nano Lett.* **16**, 5836 (2016).
- ¹⁰ D. Çakır, F. M. Peeters, and C. Sevik, Mechanical and thermal properties of h-MX₂ (M=Cr, Mo, W; X=O, S, Se, Te) monolayers: A comparative study. *Appl. Phys. Lett.* **104**, 203110 (2014).
- ¹¹ S. P. Koenig, N. G. Boddeti, M. L. Dunn, and J. S. Bunch, Ultrastrong adhesion of graphene membranes, *Nat. Nanotech.* **6**, 543 (2011).

-
- ¹². A. Berkdemir, H. R. Gutiérrez, A. R. Botello-Méndez, N. Perea-López, A. L. Elías, C.-I. Chia, B. Wang, V. H. Crespi, F. López-Urías, J.-C. Charlier, H. Terrones, and M. Terrones, Identification of individual and few layers of WS₂ using Raman Spectroscopy, *Sci. Rep.* **3**, 1755 (2013).
- ¹³. W. Zhao, Z. Ghorannevis, K. K. Amara, J. R. Pang, M. Toh, X. Zhang, C. Kloc, P. H. Tane, and G. Eda, Lattice dynamics in mono- and few-layer sheets of WS₂ and WSe₂, *Nanoscale* **5**, 9677 (2013).
- ¹⁴. H. Malekpour, and A. Balandin, Raman-based technique for measuring thermal conductivity of graphene and related materials, *J. Raman Spectrosc.* **49**, 106 (2018).
- ¹⁵. D. Tedeschi, E. Blundo, M. Felici, G. Pettinari, B. Liu, T. Yildirim, E. Petroni, C. Zhang, Y. Zhu, S. Sennato, Y. Lu, and A. Polimeni, Controlled Micro/Nanodome Formation in Proton-Irradiated Bulk Transition-Metal Dichalcogenides, *Adv. Mat.* (2019), in press, DOI: 10.1002/adma.201903795
- ¹⁶. C. Robert, D. Lagarde, F. Cadiz, G. Wang, B. Lassagne, T. Amand, A. Balocchi, P. Renucci, S. Tongay, B. Urbaszek, and X. Marie., Exciton radiative lifetime in transition metal dichalcogenide monolayers, *Phys. Rev. B* **93**, 205423 (2016).
- ¹⁷. Y. Sun, S. E. Thompson, and T. Nishida, *Strain Effect in Semiconductors: Theory and Device Applications*, Ch. 2 (Springer New York, 2010).
- ¹⁸. J. Feng, X. Qian, and C.-W Huang, Strain-engineered artificial atom as a broad-spectrum solar energy funnel, *Nat. Photon.* **6**, 865 (2012).
- ¹⁹. Castellanos-Gomez, A.; Roldán, R.; Cappelluti, E.; Buscema, M.; Guinea, F.; van der Zant, H. S. J. & Steele, G. A. Local Strain Engineering in Atomically Thin MoS₂. *Nano Lett.* **13**, 5361 (2013).
- ²⁰ X. He, H. Li, Z. Zhu, Z. Dai, Y. Yang, P. Yang, Q. Zhang, P. Li, U. Schwingenschlogl, and X. Zhang, Strain engineering in monolayer WS₂, MoS₂, and the WS₂/MoS₂ heterostructure, *Appl. Phys. Lett.* **109**, 173105 (2016).

-
- ²¹ R. Frisenda, M. Drüppel, R. Schmidt, S. M. de Vasconcellos, D. P. de Lara, R. Bratschitsch, M. Rohlfing, and A. Castellanos-Gomez, Biaxial strain tuning of the optical properties of single-layer transition metal dichalcogenides. *2D Materials* **4**, 10 (2017).
- ²² H. Shi, H. Pan, Y.-W. Zhang, and B. I. Yakobson, Quasiparticle band structures and optical properties of strained monolayer MoS₂ and WS₂, *Phys. Rev. B* **87**, 155304 (2013).
- ²³ C.-H. Chang, X. Fan, S.-H. Lin, and J.-L. Kuo, Orbital analysis of electronic structure and phonon dispersion in MoS₂, MoSe₂, WS₂, and WSe₂ monolayers under strain, *Phys. Rev. B* **88**, 195410 (2013).
- ²⁴ Z. Jin, X. Li, J. T. Mullen, and K. W. Kim, Intrinsic transport properties of electrons and holes in monolayer transition-metal dichalcogenides, *Phys. Rev. B* **90**, 045422 (2014).
- ²⁵ M. Ghorbani-Asl, S. Borini, A. Kuc, and T. Heine, Strain-dependent modulation on conductivity in single-layer transition-metal dichalcogenides. *Phys. Rev. B* **87**, 235434 (2013).
- ²⁶ B. Amin, T. P. Kaloni, and U. Schwingenschl, Strain engineering of WS₂, WSe₂, and WTe₂, *RCS Adv.* **4**, 34561 (2014).
- ²⁷ H. J. Conley, B. Wang, J. I. Ziegler, R. F. Haglund Jr., S. T. Pantelides, and K. I. Bolotin, Bandgap engineering of strained monolayer and bilayer MoS₂, *Nano Lett.* **13**, 3626 (2013).
- ²⁸ S. B. Desai, G. Seol, J. S. Kang, H. Fang, C. Battaglia, R. Kapadia, J. W. Ager, J. Guo, and A. Javey, Strain-induced indirect to direct Bandgap transition in multilayer WSe₂, *Nano Lett.* **14**, 4592 (2014).